Baghdad Science Journal

Volume 23 | Issue 4 Article 25

4-28-2026

Utilization of Natural Pumice Stone as a Low-Cost Ion Exchanger for Lead (Pb(II)) Removal: A Kinetics, Isotherms and Mechanisms Studies

Ahmad Sulaiman
Department of Chemistry, Faculty of Science, University of Tartous, Tartous, Syria,
a.suliman.m.j@gmail.com

How to Cite this Article

Sulaiman, Ahmad (2026) "Utilization of Natural Pumice Stone as a Low-Cost Ion Exchanger for Lead (Pb(II)) Removal: A Kinetics, Isotherms and Mechanisms Studies," *Baghdad Science Journal*: Vol. 23: Iss. 4, Article 25.
DOI: https://doi.org/10.21123/2411-7986.5280

BAGHDAD SCIENCE JOURNAL 2026;23(4):1473–1489

Scan the QR to view
the full-text article on
the journal website

RESEARCH ARTICLE

Utilization of Natural Pumice Stone as a Low-Cost Ion Exchanger for Lead (Pb(II)) Removal: A Kinetics, Isotherms and Mechanisms Studies

Ahmad Sulaiman

Department of Chemistry, Faculty of Science, University of Tartous, Tartous, Syria

ABSTRACT

Pumice is one of the raw materials that is widely available, especially in the "Middle East region and Turkey". In this research, an ion exchanger was prepared from Syrian pumice by converting it into a low-silica ion exchanger (P_{Na}) for the removal of Pb^{2+} ions from aqueous solutions, by several chemical and hydrothermal methods with NaOH. The prepared exchanger was also characterized using a number of distinctive techniques in this paper such as (XRD, FT-IR, BET, DTA) which demonstrated radical changes in structure after modification, the most important of which are: The surface area increased approximately 18-fold from (5 to 93) m^2/g, along with an increase in relative density and a significant improvement in exchange-adsorption capacities. Maximum Pb^{2+} uptake was 4.3 mmol/g (308.15 K). Removal efficiency was 100% at low concentrations and >80% at medium/high concentrations. The adsorption kinetics followed a pseudo-first-order model, and the equilibrium data fit well to Langmuir, Freundlich, and Redlich-Peterson isotherms ($R^2 > 0.99$).

Keywords: Adsorption isotherm, Exchange-adsorption capacities, Ion exchanger, Pumice, Removal coefficients, Surface area

Introduction

Syria's geology is rich in minerals like bentonite, zeolite, and pumice, extracted by the General Establishment for Geology and Mineral Resources. These accoutrements are valued for their face parcels in separation and sanctification processes.[1,2] Among them, pumice stands out—a stormy mineral with low viscosity (0.35–0.65) g/ cm^3 and high external porosity.[3] While historically used in construction for its separating parcels,[4] its high silica (65–70)% and alumina (12–18)% content make it technically promising. Yet, lower than 3% is presently used in similar operations.[5,6] The toxin of lead ions (Pb^{2+}), which damages kidney tissue and nerve cells, drives this exploration.[6–8]

Pumice stone does not naturally provide a high surface area and cation exchange capacity,[1–3] so I chemically modified it using NaOH to improve its selectivity for Pb^{2+}. This treatment dissolves and restructures silica, creating active spots ($\equiv$Si–O^-Na^+) that enhance adsorption and exchange.[9]

As a result, pumice becomes a low-cost and sustainable option compared to activated carbon,[2] avoiding the dispersion and swelling problems that materials like bentonite suffer from.[1] Its porous structure and mechanical strength support its use in water treatment.[3–5]

The aim of this study is to develop a thermo- hydrothermal revision protocol for low- silica Syrian pumice, characterize its structure, and dissect superemінent adsorption mechanisms through kinetic, isothermal, and thermodynamic modeling.

- Creation and development of an ion exchanger from Syrian pumice modified with "NaOH"

Received 8 May 2025; revised 13 September 2025; accepted 11 October 2025.

E-mail address: a.suliman.m.j@gmail.com (A. Sulaiman).

https://doi.org/10.21123/2411-7986.5280

through colorful thermal and hydrothermal treatments.

- Evaluation of the performance of this exchanger in removing lead ions from waterless results under different conditions. The raw and modified accoutrements were also characterized using several ultramodern ways (XRD, FT- IR, BET, DTA).
- Evaluating the performance of the modified material in removing lead ions (Pb^{2+}) from aqueous solutions under varying conditions.
- Modeling the adsorption process using kinetic, isotherm, and thermodynamic models to identify the dominant mechanism and process characteristics.
- Comparing the performance of the prepared material with other reported adsorbents to confirm its viability and efficiency.

It is anticipated that this study will demonstrate that chemically modified Syrian pumice is not only a low-cost and sustainable alternative but also a high-performance material capable of competing with conventional adsorbents in treating water contaminated with heavy metals, thereby contributing to sustainable environmental solutions.

Material and methods

Material

In order to determine the percentages of oxides that entered the pumice's composition, an X-ray fluorescence spectroscopy device (XRF-1800) made by the Japanese company (LAB-Center) was used to conduct a characterization study on raw pumice before preparation, after treatment, and after drying (prepared exchanger). A volumetric nitrogen adsorption device, Gemini Micromeritics III2375 USA, was used to measure the surface area, pore radius, and average pore volume of raw pumice and exchanger (treated pumice) at -196°C. Additionally, a particle size measuring device type (Sampler Sight-Pharma Particles) was used to determine the distribution of particle size according to its dimensions.

With the aid of XRD technology and a spectroscopic analysis instrument for measuring X-ray diffraction manufactured by the Dutch business (Philips), Xpert-high score, the nature of the phases generated in the raw and sodium hydroxide-treated pumice samples was ascertained. With a differential thermal analysis-gravimetric device (DTA-TG), the thermal effects that transpired in the sample were investigated at a heating rate of 10°C/min up to 850°C and in the range of (20-850)°C. It is a STA PT-1600 device manufactured in Germany by LINSEIS. The use of a 250μl aluminium sink and temperatures between 20 and 1000°C were used for the job. A JASCO 4100 FT-IR spectrometer operating in the 400–4000 cm^{-1} range was used to analyze the FT-IR spectra of the Raw Pumice P_{raw} and the Product Exchanger P_{Na} using the disc method. The sample was made by compressing the sample/KBr mixture at a pressure of 5 × 10-3 kg/cm^2 and a ratio of (sample/KBr = 200/1). In addition to the raw material, raw pumice from the Southern Region of Syria, the following chemicals were used in the study: CH_3COOH, CH_3COONa, NaOH, EDTA, $Pb(NO_3)_2$, and indicators (Xylenol orange) made by "RIEDEL-DE HAEN," Hexamine, acid buffer solution (Ph = 5–6), and double distilled water (1.5–3μs).

Methods of preparing ion exchangers

The following procedures were used to prepare the exchanger: raw pumice was treated with sodium hydroxide to achieve the appropriate shape:

- ➢ Raw pumice was ground to a particle size of 200–300 μm. 6.0 g of raw pumice and 7.2 g of sodium hydroxide were combined in a porcelain crucible and placed in a thermal incinerator set to 600°C for two hours. The product was then cooled, crushed, and heated with stirring under reflux distillation until it boiled for 72 hours.
- ➢ To get the required ion exchanger P_{Na}, the product is transferred to an autoclave and heated to 140°C for 72 hours, after which it is cleaned, filtered, and dried at 105°C.[9]

Study design and characterization

This study involved a descriptive analysis of the raw sample (P_{raw}) and the final exchanger (P_{Na}), examining physical parameters through characterization techniques. X-ray diffraction (XRD), X-ray fluorescence (XRF), volumetric gas adsorption, particle size analysis, and differential thermal analysis-thermogravimetry (DTA-TG) were used to determine structural identity.

Relative density measurement

A precise mass (m) of the dried exchanger (105°C) was placed in a volumetric flask, followed by the addition of kerosene (non-miscible organic liquid) to displace air bubbles and fill the flask. The sample volume was derived from the liquid displacement difference, and density was calculated using the standard formula by Eq. (1).[10]

$$D = \frac{m}{V}\ g/cm^3. \tag{1}$$

Swelling water

The swelling water (W) was determined by measuring the mass difference between the water-saturated exchanger (m*) and the dry sample (m, dried at 105°C to constant weight). The capacity was calculated by Eq. (2):[11]

$$W = \frac{m^* - m}{m}\ gH_2O/g. \tag{2}$$

Exchange-adsorption capacity

Samples of the exchanger (m = 1.0–3.0 g) were immersed in 100 mL $Pb(NO_3)_2$ solutions (M_0 = 0.00625-0.15 mol/L) for 48 h at 298.15, 303.15, and 308.15 K. Initial and equilibrium concentrations were determined by EDTA titration using appropriate indicators and pH control.[12] The exchange-adsorption capacity (q_e) was calculated by Eq. (3):[12,13]

$$q_e = \frac{(M_0 - M_e) \times V}{m} mmol/g. \tag{3}$$

Where (M_0) initial concentration (mol/L), (M_e) equilibrium concentration (mol/L), (q_e) exchange-adsorption capacity (mmol/g),(V) Soaking solution volume (100mL).

Removal coefficient

Based on the relationship (4), the removal coefficient of the ion was investigated as a function of the mass of the exchanger added to 100 (mL) of the investigated ion solution with a fixed initial concentration.[14]

$$R\% = \frac{(M_0 - M_e)}{M_0} \times 100\%. \tag{4}$$

Where (R) is the removal coefficient (%).

Kinetic and isotherm studies

The Pb(II) adsorption kinetics were evaluated using pseudo-first-order (PFO) and pseudo-second-order (PSO) models.[15] The PFO model is expressed by Eq. (5):

$$\frac{dq_t}{q_t} = k_1\left(q_e - q_t\right). \tag{5}$$

where (q_t) is the adsorption capacity at the specified time (mmol/g), (q_e) is the equilibrium capacity (mmol/g), and K_1 is the rate constant per hour (h^{-1}). To determine the value of K_1, a plot of log ($q_e - q_t$) against time (t) is drawn. After integrating Eq. (5) between the limits, t = 0 to t = t and q_t = 0 to $q_t = q_e$, we obtain by Eq. (6):

$$\log\left(q_e - q_t\right) = \log(q_e) - \frac{k_1}{2.303}t. \tag{6}$$

The pseudo-second-order model postulated that chemisorption, which involves ion exchange or functional groups, was the primary rate-limiting phase between the adsorbent and the adsorbate, group chelation.[16] The non-linear and the formulas for the linear model were provided Eqs. (7) and (8).

The Pseudo-second-order PSO model[17] can be written by Eq. (7):

$$\frac{dq_t}{dt} = K_2(q_e - q_t)^2. \tag{7}$$

where $K2$ is the equilibrium rate constant of the PSO model ($g.mmol^{-1}.h^{-1}$). Separating the variables in Eq. (7) and integrating for the boundary conditions $q_t = 0$ to $q_t = q_t$ and $t = 0$ to $t = t$ yields an expression that may be rearranged into the following linear form Eq. (8):

$$\frac{t}{q_t} = \frac{1}{K_2 \times q_e^2} + \frac{1}{q_t}t. \tag{8}$$

The effect of contact time in the range of (4–48) hours (every four hours) and kinetics at three temperatures (298.15, 303.15, 308.15) K, and the concentration is 0.10 mol/L

Equilibrium isotherms modelling

The Pb^{2+} adsorption data were fitted to nine isotherm models (Radlich-Peterson, Langmuir, Freundlich, Halsey, Temkin, Harkins-Jura, Dubinin, Janovic, and Henry) using Sorption Analysis.[18] Based on correlation coefficients (R^2), seven models showed excellent agreement with experimental data, with Radlich-Peterson, Langmuir, Freundlich, Halsey, Temkin, Harkins-Jura, and Dubinin isotherms demonstrating the best fit (R^2 closest to 1).

Harkins-Jura isotherm

The Harkins-Jura isotherm, originally developed for gas-phase adsorption,[19] has been successfully adapted to liquid-solid systems.[20] This model accounts for multilayer adsorption on heterogeneous surfaces with non-uniform pore distribution, as described by Eq. (9).[20]

$$\frac{1}{q_e^2} = \left[\frac{B}{A}\right] - \frac{1}{A}\log\left(C_e\right). \tag{9}$$

where (C_e) is the equilibrium concentration of the sorbate in the liquid phase ($mmol.l^{-1}$), (q_e) is the equilibrium adsorption capacity ($mmol.g^{-1}$), (A) and (B) are constants of Harkins-Jura, obtained from the plot of $^1/_{q_e^2}$ against log (C_e).

Freundlich isotherm

The Freundlich isotherm describes multilayer adsorption on heterogeneous surfaces and is widely applied for ion removal from aqueous solutions.[21] This empirical model indicates that adsorption capacity increases with surface site energy heterogeneity, favoring high-energy active sites.[22] The Freundlich equation is expressed by Eq. (10):

$$q_e = K_F \times (C_e)^{\frac{1}{n}}. \tag{10}$$

This equation is also given in logarithmic form by the following relation by Eq. (11):[22]

$$\log(q_e) = \log\left(K_F\right) + \frac{1}{n}\log\left(C_e\right). \tag{11}$$

where (C_e) is the equilibrium concentration of the sorbate in the liquid phase ($mmol.l^{-1}$), (q_e) is the equilibrium adsorption capacity ($mmol.g^{-1}$), (K_F) is the Freundlich constant ($l.g^{-1}$), and (n) is a constant at a given temperature and it is dependent on the nature of the adsorbate and the adsorbent.

Langmuir isotherm

When the adsorption centers have equal strengths, the Langmuir model describes the adsorbent's monolayer adsorption. There are specific equal areas on the surface of adsorbents that are conducive to adsorption, according to the isothermal equation theory. The materials' adhesion surfaces have the same kind of energy for this process, according to the Langmuir equation.[23] The following relation provides the Langmuir equation by Eq. (12).[22]

$$q_e = \frac{q_{max} \times K_L \times C_e}{1 + K_L \times C_e}. \tag{12}$$

where (q_e) is the equilibrium adsorption capacity ($mmol.g^{-1}$), (q_{max}) is the maximum adsorption capacity ($mmol.g^{-1}$), is the equilibrium adsorption capacity ($mmol.g^{-1}$), (C_e) is the equilibrium concentration of the sorbate in the liquid phase ($mmol.l^{-1}$), (K_L) is the Langmuir constant ($l.mmol^{-1}$), (q_{max}) and (K_L) are Langmuir constants related to adsorption capacity and rate of adsorption. The linearized Langmuir model is represented by Eq. (13) :

$$\frac{C_e}{q_e} = \frac{1}{q_{max} \times K_L} + \frac{1}{q_{max}}C_e. \tag{13}$$

By plotting C_e/q_e against C_e, it was possible to obtain the value of q_{max} from the slope, which was $1/q_{max}$, and the value of K_L from the intercept, which was $1/(q_{max}.K_L)$. The Langmuir plots for Pb^{2+} ion isothermal adsorption data were drawn. It shows that the Langmuir adsorptive isothermal equation matches the experimental results closely. The correlation coefficients were found to be greater than 0.99.

Temkin isotherm

The Temkin model expresses the linear decrease in the heat of adsorption with a uniform distribution of specific energy.[23] This isotropic model calculates the value of the heat of absorption (B) by drawing the relationship by plotting ($\ln C_e$) against (q_e) in Eq. (14).[12]

$$q_e = B\ lnA_T + BlnC_e. \tag{14}$$

Where (B) $= RT/b_T$; (R) is the universal gas constant (8.314 $J.\ mol^{-1}.K^{-1}$), and T is the absolute temperature (K). The constants of the equation can be determined as mentioned previously by drawing the relationship by drawing the relationship by plotting ($\ln C_e$) against (q_e) in Equation. From the slope, we calculate the value of the constant (B) and find the value of the constant b_T, and from the intercept, we can calculate the constant A_T.

Dubinin–Radushkevich isotherm (D-R)

Another semi-empirical model that is derived from the micropore filling theory is the Dubinin-Radushkevich model, which is frequently used to show that the adsorption process is on a non-homogeneous surface with a Gaussian energy distribution.[24] Traditionally, this method has been employed to differentiate between chemical and physical dye adsorption. The following relation provides the Dubinin-Radushkevich by Eq. (15).[12]

$$q_e = q_{DR}exp^{-k\varepsilon^2}. \tag{15}$$

This equation is also given in logarithmic form by the following relation Eq. (16).

$$lnq_e = lnq_{DR} - K_{DR}\varepsilon^2. \tag{16}$$

Where(q_{DR}) is the maximum adsorption capacity ($mmol.g^{-1}$), (qe) is the equilibrium adsorption capacity ($mmol.g^{-1}$), (K_{DR}) is the Dubinin-Radushkevich constant and related to sorption energy($mol^2.kJ^{-2}$), (ε) is the polanyi potential ($kJ.mol^{-1}$), which is equal to Eq. (17). We calculate the value of the constant (K_{DR}) from the slope, and we find the value of the constant (q_{DR}), from the intercept by Eq. (17).

$$\varepsilon = RT \ln\left(1 + \frac{1}{C_e}\right). \tag{17}$$

Where (R) is the gas constant ($kJ.mol^{-1}K^{-1}$) and (T) is the absolute temperature (Kelvin), (C_e) is the equilibrium concentration of the sorbate in the liquid phase ($mmol.l^{-1}$), The Dubinin-Radushkevich (D-R) equation can be used to calculate the energy of adsorption (E_{ads}) from the value of (K_{DR}) from the following Eq. (18).[25]

$$E_{ads} = \frac{1}{\sqrt{2K_{DR}}}. \tag{18}$$

Halsey isotherm

The Halsey adsorption isotherm is suitable for multilayer adsorption, and its equation is given by the following relation by Eq. (19).[26]

$$lnq_e = \frac{1}{n}lnK - \frac{1}{n}lnC_e. \tag{19}$$

Where (C_e) is the equilibrium concentration of the sorbate in the liquid phase ($mmol.l^{-1}$), (q_e) is the equilibrium adsorption capacity ($mmol.g^{-1}$), (n and k) are Halsey adsorption isotherm constants determined by plotting (ln q_e) against (ln C_e), and from the slope we can calculate the value of the constant (n), and we can calculate the value of the constant (k) from the intercept.

Janovich isotherm

Based on the Janovich model, the Langmuir model is assumed to be suitable for the adsorption process. However, it is considered that there are important interactions between the adsorbent and the sorbent, which are not taken into account by the Langmuir equation. The Janovich equation is shown in Eq. (20).[27]

$$q_e = q_m\left(1 - e^{K_jC_e}\right). \tag{20}$$

The logarithmic form of the previous relationship is given by Eq. (21)

$$lnq_e = lnq_m - k_jC_e. \tag{21}$$

Where (q_m) is the theoretical adsorption capacity ($mmol.g^{-1}$), (q_e) is the equilibrium adsorption capacity ($mmol.g^{-1}$), (C_e) is the equilibrium concentration of the sorbate in the liquid phase ($mmol.l^{-1}$), (K_j) is Janovich's constant, which is determined from the slope, by plotting ln (q_e) against (C_e), and (q_m) may be determined from the intercept.[28]

Redlich-Peterson isotherm

The Redlich-Peterson isotherm is the result of combining the Freundlich and Langmuir isotherms. The adsorption mechanism assumes that adsorption takes place in many levels, even though it is a mixture. This isotherm equation is given by Eq. (22).[12,28]

$$ln\frac{C_e}{q_e} = \beta lnC_e - lnA. \tag{22}$$

Where (C_e) is the equilibrium concentration of the sorbate in the liquid phase ($mmol.l^{-1}$), (q_e) is the equilibrium adsorption capacity ($mmol.g^{-1}$) (β and A) are Redlich-Peterson constants, which are determined by plotting (ln C_e/q_e) against (ln C_e), and from the slope, we can calculate the value of the constant (β), and we can calculate the value of the constant (A) from the intercept.[27]

Henry's isotherm

This is known as the simplest adsorption isotherm. At almost every concentration, this isotherm is true. It increases the adsorbate's adsorption capacity by increasing its surface area. Henry's isotherm formula is provided in Eq. (23).[22]

$$q_e = K_HC_e. \tag{23}$$

Where (q_e) is the equilibrium adsorption capacity ($mmol.g^{-1}$), (C_e) is the equilibrium concentration of the sorbate in the liquid phase ($mmol.l^{-1}$), (K_H) are Henry's constant, which is determined by plotting (q_e) against (C_e), and from the slope, we can calculate the value of the constant (K_H).[29]

Thermodynamics studies

The effect of temperature on adsorption was studied. The experiment was carried out at three different temperatures (298, 303, 308) K and at different concentrations and doses. In order to calculate the thermodynamic constants, the Gibbs-free energy change ($\Delta G°$), entropy change ($\Delta S°$), and enthalpy change ($\Delta H°$) were determined at the above temperatures and for a fixed weight of 1g and a concentration of (0.1 mol/l), and could be determined according to

Table 1. Shows the chemical composition of Raw Pumice and sodium hydroxide treated pumice by XRF.

Sample	Chemical Composition									
Pumice	SiO_2	Al_2O_3	Fe_2O_3	CaO	MgO	SO_3	K_2O	Na_2O	LOI	Sum
P_{raw}	42.74	14.95	19.00	9.11	5.97	0.00	1.71	3.42	1.48	98.38
P_{Na}	33.40	13.41	17.68	8.32	5.43	0.00	0.76	9.26	10.18	98.44

the following Eq. (24).[30]

$$\Delta G^\circ = -RTlnK_c. \tag{24}$$

Where (T) is the temperature (K), K_C (q_e/C_e) is the equilibrium constant, (R) is the universal gas constant (8.314 J/mol K), and (ΔG°) is the Gibbs-free energy change. The entropy change (ΔS) and enthalpy change (ΔH°), parameters were estimated from the following by Eqs. (25) and (26).[12]

$$lnK_C = \frac{\Delta S^\circ}{R} - \frac{\Delta H^\circ}{RT}. \tag{25}$$

$$\Delta G^\circ = \Delta H^\circ - T\Delta S^\circ. \tag{26}$$

The values of (ΔH°) and (ΔS°) can be obtained from the slope and intercept of a plot of (ln K_c) against (1/T).

Results and discussion

Table 1 shows that the pumice contains43.00 wt% SiO_2 (low compared to global samples, where SiO_2 typically exceeds70.00 wt%), along with15.00 wt% Al_2O_3, 19 wt% Fe_2O_3, 9.11 wt% CaO, 5.97 wt% MgO, 3.12 wt% Na_2O, 1.21 wt% K_2O, and no sulfur.[31] After thermal/hydrothermal treatment with NaOH, SiO_2 drops to 33.40 wt%, while Al_2O_3, Fe_2O_3, CaO, MgO, and K_2O slightly decrease. The burning loss increases from 1.48 wt% (raw) to10.18 wt%, and Na_2O rises to 9.26 wt%.[31–33]

Nitrogen physisorption (−196 °C) revealed a dramatic 18-fold increase in S_{BET} (from 5 m^2/g for raw pumice, P_{raw}, to 93 m^2/g after NaOH treatment, P_{Na}), indicating mesopore formation (2–50 nm).[34,35] This textural enhancement correlated with improved adsorption: P_{Na} showed significant capacity vs. negligible uptake for P_{raw}, due to silica framework dissolution via the reaction.[36]

$$\mathbf{SiO_2 + 2NaOH \rightarrow Na_2SiO_3 + H_2O}$$

This process generates water-soluble sodium silicate, increasing porosity through:

- **Restructuring** of the aluminosilicate network at 80–120 °C;[37]
- **Formation** of active exchange sites ($\equiv$Si–O^-Na^+);
- **Development** of a mesoporous structure optimal for large-molecule adsorption.[37]

Modified pumice exhibited 90% higher adsorption capacity for Cd^{2+} and Pb^{2+} versus raw material,[38] demonstrating NaOH treatment's efficacy for producing high-performance adsorbents. Nitrogen physisorption (-196°C) revealed P_{Na} surface area (S_{BET}) increased dramatically from 5 m^2/g (P_{raw}) to 93 m^2/g, with pore expansion into the mesoporous range.[33] This textural enhancement correlated with significantly improved ion-exchange capacity (negligible in P_{raw} vs. high in P_{Na}),[39] and Table 2. shows the most important surface data for both P_{raw} and P_{Na}.

Table 2. Shows the specific surface areas, average pore radius, and pore volume of the raw Pumice (P_{raw}), and prepared ion exchanger (P_{Na}).

	Sample Pumice	
S_{BET}	P_{raw}	P_{Na}
$S_{BET}(m^2/g)$	5.1	93.0
$\overline{r_a}$(nm)	1.47	3.08
V_T(ml/g)	0.0076	0.1437

(S_{BET}): surface area, (r_a^-) :average pore radius, (V_T) total pore volume.

XRD analysis of P_{raw} and P_{Na} Figs. 1 and 2 revealed crystalline phases through Bragg's law (nλ =2dsinθ).[40] P_{raw} contained primarily dachiardite, with Analcime, Feldspar, and Chabazite (zeolitic mineral), evidenced by peaks at 2θ =20-60° and a distinct quartz peak at 26.60° Fig. 3.

In addition, Dachardite: $(Ca,Na_2)_2{\cdot}Al_4Si_{20}O_{48}{\cdot}13H_2O$, Analcim:$(Na_2O{\cdot}Al_2O_3{\cdot}4SiO_2{\cdot}2H_2O)$ d = 5.61, 3.43, 2.43, 2.67, 2.50, 1.90, 1.87, 1.74, Philipsite: $(Ca,K,Na)_{1\text{-}2}(Al_3Si_5O_{16}){\cdot}4H_2O$ d = 7.19, 5.06, 4.13, 3.26, 3.18, 3.14, 2.70, 1.59. The samples contain similar proportions of calcite corresponding to the following absorption peaks,[41,42] d = 3.10, 2.27, 2.08, In addition Alumina, Hematite and Silica are present for treated pumice.

Under ambient pressure, SiO_2 undergoes sequential phase transformations: α-quartz (hexagonal β-quartz at 573°C) $\rightarrow$ β-tridymite (870°C) $\rightarrow$ β-cristobalite (cubic,1470°C) $\rightarrow$ molten silica (1705°C). Pure quartz bypasses tridymite, converting directly to cubic β-cristobalite at 1050°C.[42]

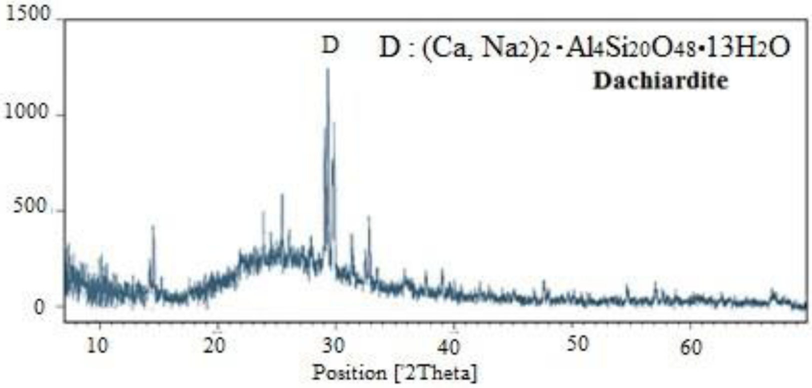

Fig. 1. Shows the XRD spectrum of raw Pumice (P_{raw}).

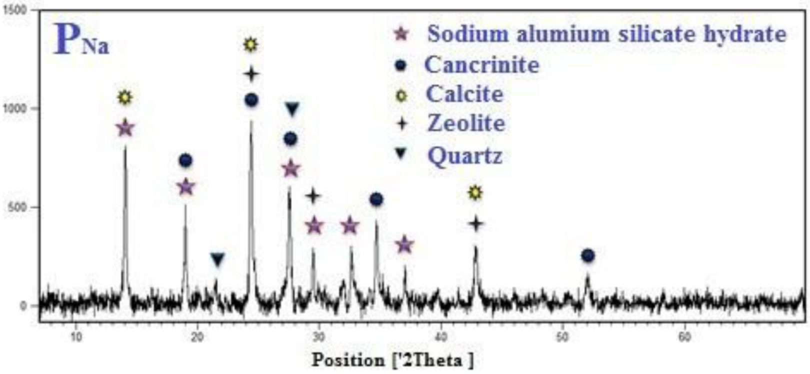

Fig. 2. Shows the XRD spectrum of the Ion exchanger (P_{Na}).

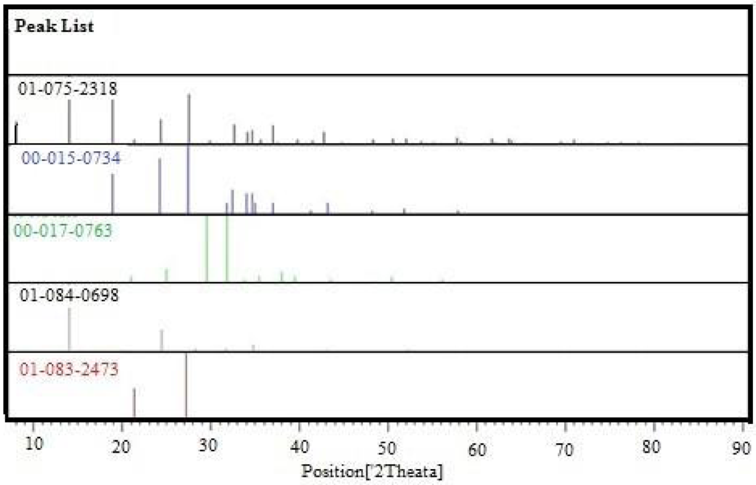

Ref. Code	Compound Name	Chemical Formula
01-075-2318	Sodium aluminum silicate hydrate	$(Na_2O)_{1.31}\ Al_2O_3\ (SiO_2)_{2.01}\ (H_2O)_{1.65}$
00-015-0734	Cancrinite, syn	$Na_4\ (Al\ Si\ O_4)_3\ (OH)$
00-017-0763	calcite-III	$CaCO_3$
01-084-0698	Zeolite ZK-14, syn	$Na_{3.68}\ Al_{3.6}\ Si_{8.4}\ O_{24}\ (H_2O)$
01-083-2473	Quartz, syn	SiO_2

Fig. 3. Shows the detailed XRD spectra corresponding to the formed crystalline phases.

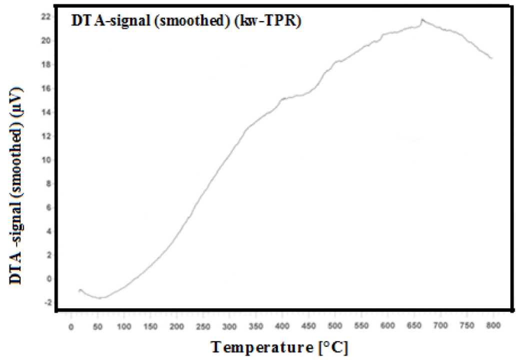

Fig. 4. Differential thermal analysis (DTA) curve of Raw Pumice (P_{raw}).

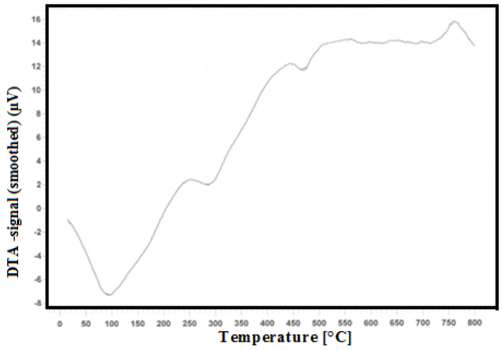

Fig. 5. Differential thermal analysis (DTA) curve of the prepared Ion Exchanger (P_{Na}).

Thermal analysis of raw and ion-exchanged Pumice

The differential thermal analysis (DTA) curve of raw pumice (Praw) Fig. 4 and Table 3 exhibits an endothermic peak at 54.2°C, corresponding to the loss of adsorbed surface moisture (∼1.00 wt%). A minor endothermic effect appears at 406.7°C (370–420°C range), attributed to the dehydration of surface OH groups, accompanied by a marginal weight loss (∼0.50 wt%). A pronounced endothermic peak at 667.8°C (640–670°C range) reflects carbonate decomposition (∼0.55 wt% loss), coinciding with the α- to β-quartz transition, and unique alumina structures, such as γ-Al2O3, are created.[43,44] Total weight loss at 850°C reached ∼2.30 wt%, consistent with pumice sintering, while melting occurs at 1200°C.[43,44]

For the ion-exchanged pumice (P_{Na}), the DTA curve Fig. 5 and Table 3 shows a distinct endothermic peak at 92.0°C (50–250°C range) due to adsorbed water loss (∼4.00 wt%). A secondary peak at 285.3°C (250–310°C range) signifies the removal of chemically bound water (∼1.27 wt%), followed by OH group dehydration at 510°C (470–550°C range, ∼3.00 wt% loss). The α- to β-quartz transition was again observed.[43,44] An exothermic peak at 800°C indicates recrystallization, with total weight loss at 850°C amounting to ∼11.32 wt%.

FTIR spectral analysis

Table 4 and Fig. 6 show the characteristic absorption bands of all samples. FTIR analysis revealed

Table 3. Shows the percentage of loss by burning for the pumice sample (P_{raw}) and the prepared ion exchanger (P_{Na}).

	Calculate the percentage of loss due to burning of Pumice	
	$P_{(Na)}$	P_{raw}
Temperature	Loss percentage%	Loss percentage%
100°C	4.000%	1.000%
200°C	4.270%	1.091%
400°C	6.906%	1.701%
600°C	9.210%	2.251%
800°C	11.329%	2.300%
1000°C	11.320%	2.300%

Table 4. Infrared Spectral Peaks FT-IR of raw Pumice and prepared ion exchanger (PNa).

Wavenumber (cm^{-1})	Assignment	References
∼3450	O–H stretching (H_2O)	45–47
∼1630	H–O–H bending (H_2O)	47–49
1770–1850	Overtones/combinations (raw pumice only)	46,50
1430–1460	CO_3^{2-} bending (treated pumice only)[a]	46,50
∼1030	Si–O–Si asymmetric stretching[b]	45–47,51
666 → 624–684	Si–O–Al / quartz vibrations[c]	52–54
∼450–460	Si–O bending	45,46,51,52

[a] Appearance of this band indicates surface carbonation from atmospheric CO_2 or calcite impurities.
[b] Persistence of this band confirms preservation of the silicate backbone.
[c] Shift and broadening of this band suggests structural framework rearrangement.
Note: O–H bands (∼3450, ∼1630 cm^{-1}) indicate adsorbed water, typical for porous materials.

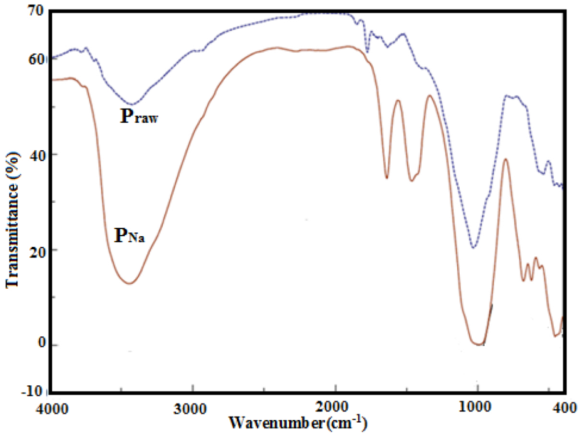

Fig. 6. Shows the FT-IR spectra of Raw Pumice (P_{raw}), and the prepared exchanger (P_{Na}).

Table 5. Relative density of Raw Pumice (P_{raw}), and the prepared Ion Exchanger (P_{Na}).

Processed Form	Exchange Code	Relative density(g/cm^3)
Untreated Pumice (raw)	P_{raw}	1.45
Basically treated Pumice	P_{Na}	2.38

Table 6. Represents the values of swelling water (W) gH_2O/g, for Raw Pumice (P_{raw}), (P_{Na}).

Processed Form	Exchange Code	swelling water (gH_2O/g)
Untreated Pumice (raw)	P_{raw}	0.18
Basically treated Pumice	P_{Na}	1.28

characteristic absorption bands that indicate the molecular composition of the samples.

Density and surface properties of raw and naoh-treated Pumice

Based on Table 5, the density of raw pumice is 1.45 g/cm^3, and the P_{Na} exchanger is 2.38 g/cm^3. It is inferred from Table 2 that the raw pumice has low porosity due to its low surface area. After the revision process, the density increased significantly due to its accession of a conspicuous pervious structure. This significant change is due to the dissolution of silica and a structural rearrangement of the structure,[53,54] in addition to the increase in the quantum of swelling water after the revision process to reach (1.28 gH2O/ g) Table 6, while before the treatment it was (0.18 gH2O/ g), which in turn confirms the penetration of sodium ions into the structural frame

Exchange-adsorption capacity studies

The exchange-adsorption capacity (q_e) was totally delved as a function of temperature (298.15–308.15 K), original Pb^{2+} attention (0.0125–0.15 mol/ L), and exchanger mass (1.0–3.0 g), while maintaining a constant result volume of 100 mL Figs. 7 to 9. From the above, it was found that the exchange- adsorption capacities are directly proportional to the initial concentration of Pb^{2+} ions and their equilibrium concentration. This leads to the release of a certain amount of sodium ions (Na^+) into the solution, which in turn increases the competitive effect against Pb^{2+} ions. The same applies when increasing temperature (up to a certain limit, of course), as it facilitates ion movement and reduces viscosity. In addition to the surface properties and ionic radius, all of the above factors contribute to increasing the adsorption capacities.[55]

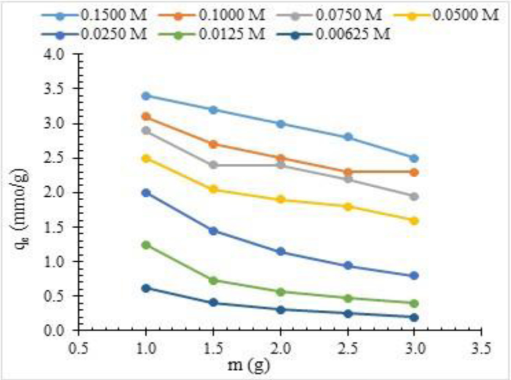

Fig. 7. The exchange-adsorption capacity of the Ion Exchanger prepared from Pumice (P_{Na}), at 298.15 K.

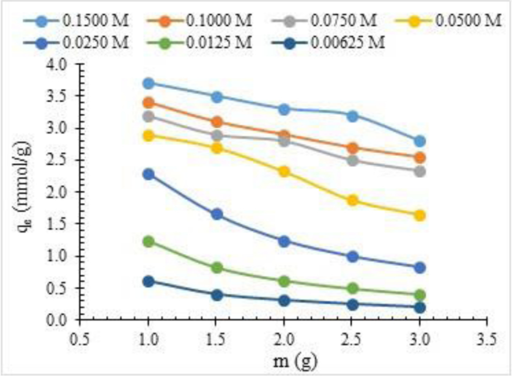

Fig. 8. The exchange-adsorption capacity of the Ion Exchanger prepared from Pumice (P_{Na}), at 303.15 K.

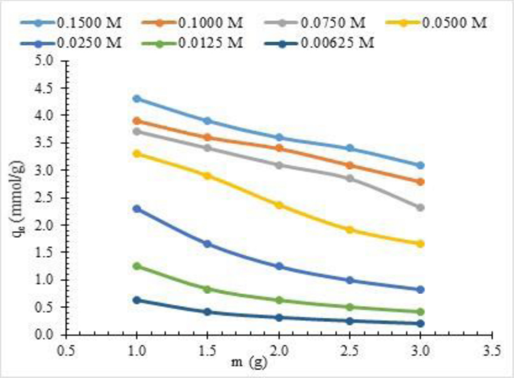

Fig. 9. The exchange-adsorption capacity of the Ion Exchanger prepared from Pumice (P_{Na}), at 308.15 K.

Removal efficiency optimization in ion exchange systems

High initial concentrations of Pb^{2+} ions and large masses result in a high removal yield (R%), leading to a greater number of replaceable sites. At low initial concentrations, where equilibrium concentrations are lower, the opposite occurs.[33,56] Furthermore, increasing temperature (within the studied range) also contributes to improved removal yield (R%). This behavior is consistent with Arrhenius-type behavior.

The inverse correlation between initial concentration and removal efficiency, as illustrated in Figs. 10 to 12, can be mechanistically interpreted in terms of geometric constraints imposed by the finite number of exchange sites per unit mass of the adsorbent, and transport barriers that become dominant at higher concentrations, where accessibility to deeper sites limits the overall exchange process.[33,56]

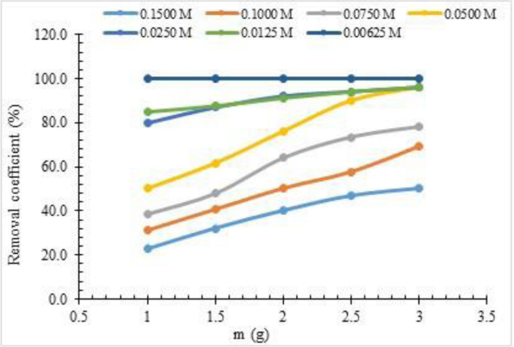

Fig. 10. The Removal Coefficient of the Ion Exchanger prepared from Pumice (P_{Na}), at 298.15 K.

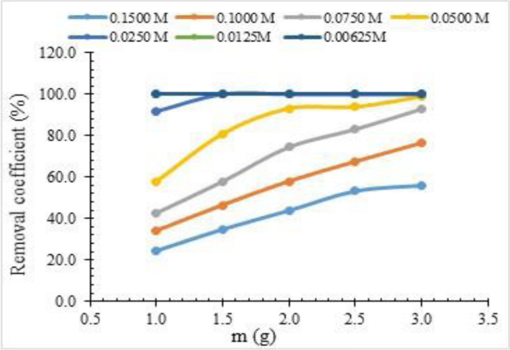

Fig. 11. The Removal Coefficient of the Ion Exchanger prepared from Pumice (P_{Na}), at 303.15 K.

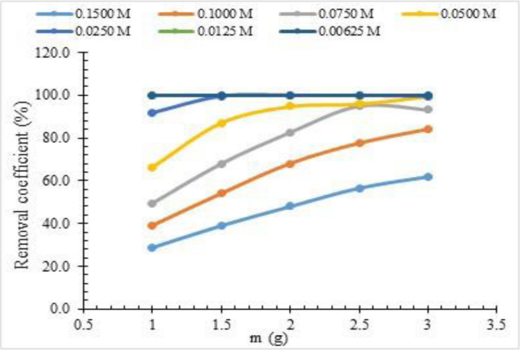

Fig. 12. The exchange-adsorption capacity of the Ion Exchanger prepared from Pumice (P_{Na}), at 308.15 K.

Applying the kinetic equations for the apparent pseudo-first-order (PFO) Eq. (6), Figs. 13 to 15, and pseudo-second-order (PSO) Eq. (8), Figs. 16 to 18 to the adsorption kinetics of the Pb (II) ion solution made it evident that the reaction's kinetics followed the apparent pseudo-first-order (PFO), which the correlation coefficient R^2 verified using Table 7 and Figs. 13 to 15.

If we look at Fig. 19, we notice the increase in exchange-adsorption capacity with the passage of time, which in turn leads to an increase in the removal efficiency R%, which is consistent with the previous Figs. 7 to 12.[57]

Table 7. Adsorption kinetics on ion exchange P_{Na}.

		Temperature	Pseudo-First Order			Pseudo-Second Order		
Ion Exchanger	Metal Ion	K(Calvin)	qe(mmol/g)	K_1(hour^{-1})	R^2	Qe (mmol/g)	K_2 (g/mg.hour)	R^2
P_{Na}	Pb^{2+}	298.15	4.540	0.059	0.95	–13.227	34×10^{-5}	0.17
		305.15	5.098	0.066	0.93	14.164	49×10^{-5}	0.44
		308.15	5.553	0.064	0.98	15.128	43×10^{-5}	0.51

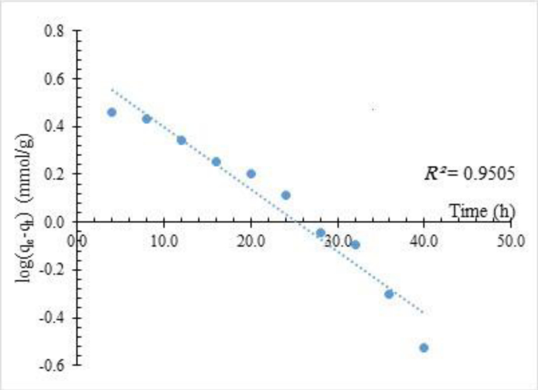

Fig. 13. Adsorption Kinetics on Ion Exchange P_{Na} Pseudo-First Order at 298.15 K.

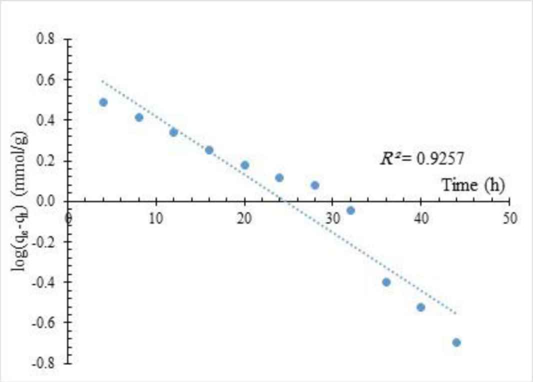

Fig. 14. Adsorption Kinetics on Ion Exchange P_{Na} Pseudo-First Order at 303.15 K.

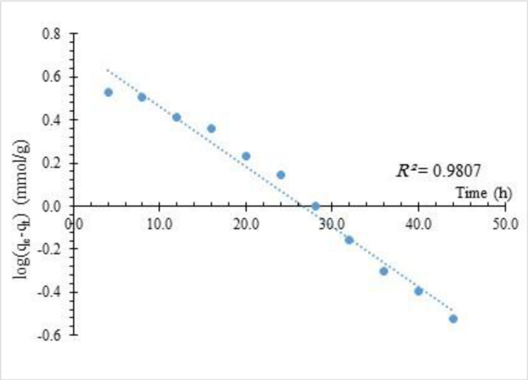

Fig. 15. Adsorption Kinetics on Ion Exchange P_{Na} Pseudo-First Order at 308.15 K.

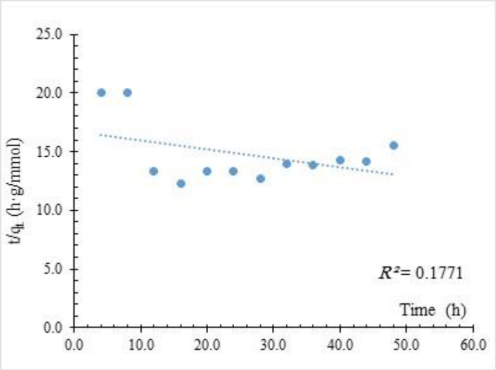

Fig. 16. Adsorption Kinetics on Ion Exchange P_{Na} Pseudo-Second Order at 298.15 K.

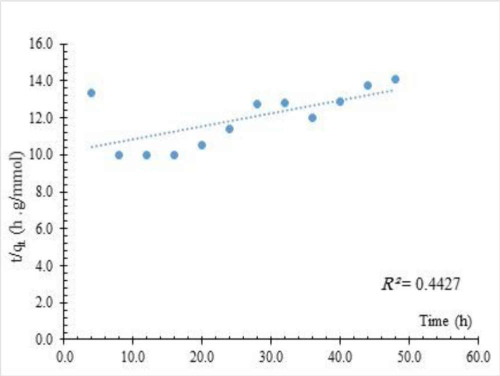

Fig. 17. Adsorption Kinetics on Ion Exchange P_{Na} Pseudo-Second Order at 303.15 K.

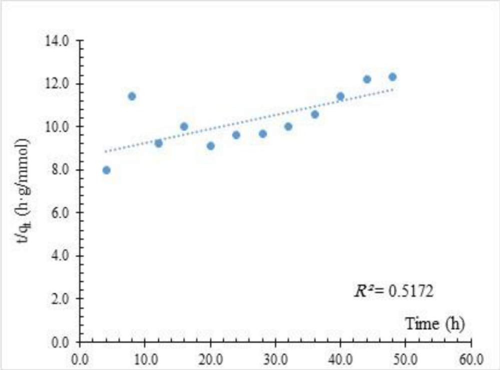

Fig. 18. Adsorption Kinetics on Ion Exchange P_{Na} Pseudo-Second Order at 308.15 K.

Table 8. Parameters calculated by Redlich-Peterson, Langmuir, Freundlich, Halsey, Temkin, Harkins-Jura, Dubinin–Radushkevich, Janovich, and Henry's isotherms from the previous equations, at temperatures T = (298.15, 303.15, 308.15) K, at a weight of (1) gr of the ion exchanger (P_{Na}) and the concentrations studied previously.

		Temperature (K)		*Redlich-Peterson Model*	
Ion Exchanger	Metal Ion	T (K)	β	A	R^2
P_{Na}	Pb^{2+}	298.15	0.831	4.870	1.00
		305.15	0.884	4.651	0.99
		308.15	0.844	6.116	0.99

Langmuir Model

		T (K)	q_{max}(mmol/g)	K_L (L/mmol)	R^2
P_{Na}	Pb^{2+}	298.15	0.29	4310.34	0.99
		305.15	3.66	390.32	0.99
		308.15	4.26	391.23	0.99

Freundlich Model

		T (K)	n	K_F	R^2
P_{Na}	Pb^{2+}	298.15	5.934	4.870	0.99
		305.15	8.658	4.651	0.99
		308.15	6.410	6.116	0.99

Halsey Model

		T (K)	n	K	R^2
P_{Na}	Pb^{2+}	298.15	–5.934	8.306×10^{-5}	0.99
		305.15	–5.934	8.306×10^{-5}	0.99
		308.15	–6.410	9.084×10^{-6}	0.99

Temkin Model

		T (K)	B(L/g)	b_T(J/mol)	A_T(L/g)	R^2
P_{Na}	Pb^{2+}	298.15	0.438	5650.37	17345.87	0.99
		305.15	0.333	7548.33	403911.06	0.96
		308.15	0.490	5224.22	49723.51	0.99

Harkins-Jura Model

		T (K)	A	B	R^2
P_{Na}	Pb^{2+}	298.15	8.196	–0.307	0.98
		305.15	14.970	–0.374	0.99
		308.15	12.6103	–0.421	0.96

Dubinin–Radushkevich (D-R) Model

		T (K)	q_{DR} (mmol/g)	K_{DR} ($mol^2.kJ^{-2}$)	E ($kJ .mol^{-1}$)	R^2
P_{Na}	Pb^{2+}	298.15	34.274	9.00×10^{-9}	7453.786	0.95
		305.15	3.745	2.00×10^{-9}	15812.776	0.94
		308.15	4.570	3.00×10^{-9}	12910.055	0.99

Janovich Model

		T (K)	q_m (mmol/g)	Kj	R^2
P_{Na}	Pb^{2+}	298.15	1.791	–6.871	0.66
		305.15	1.987	–6.921	0.56
		308.15	2.108	–8.453	0.56

Henry's Model

		T (K)	The resulting equation	R^2
P_{Na}	Pb^{2+}	298.15	$Y = 19.979\ X + 1.5229$	0.71
		305.15	$Y = 21.899\ X + 1.7157$	0.65
		308.15	$Y = 28.583\ X + 1.8491$	0.66

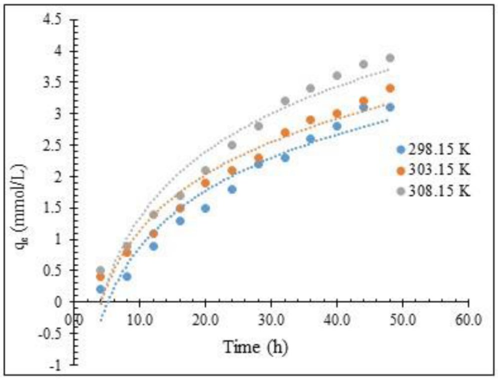

Fig. 19. Influence of contact time on adsorption of lead by ion exchanger P_{Na}.

Table 9. Thermodynamic parameters of ΔG, ΔH and ΔS for the adsorption of Lead ion exchanger P_{Na}, at temperatures of 298.15, 303.15, and 308.15 K (25, 30 and 35°C, respectively).

Temperature (k)	ΔG ($J.mol^{-1}$)	ΔH ($KJ.mol.^{-1}$)	ΔS ($KJ.mol.^{-1}.K^{-1}$)
298.15	–9432.033	–26.9132	0.1218
303.15	–9935.061		
308.15	–10652.262		

Adsorption isotherms

Of the adsorption isotherms in Table 8, the best match was Radlich-Peterson, Dubinin-Radushkevich and Langmuir, which confirms that the adsorption is monolayer and the presence of high values ($R^2 > 0.987$) confirms the presence of an interaction between the adsorbent and the adsorbate.

It is noteworthy that the Radlich-Peterson equation achieved near-perfect agreement ($R^2 \approx 1$) with experimental results.[58] This agreement is not merely numerical; it demonstrates that the adsorption mechanism does not follow a single pattern, but rather combines the behavior of the Langmuir model at low concentrations with the Freundlich characteristics at higher concentrations. This hybrid behavior reflects the complexity of the interaction occurring at the material's surface. The Timken, Halsey, and Harkins-Jura equations provided a comprehensive account of the phenomenon.[59,60]

Adsorption kinetics

The thermodynamic parameters of (ΔG), (ΔH) and (ΔS) are reported in Table 9. The (ΔG), values obtained by Eqs. (24) to (26).

The adsorption process exhibited favorable thermodynamics with $\Delta G < 0$ at all temperatures, confirming spontaneity and strong Pb(II) affinity for P_{Na}. The negative ΔH (-26.91 kJ mol^{-1})[61,62] demonstrates exothermic adsorption, while the positive ΔS (0.1218 kJ mol^{-1} K^{-1})[56,61,63] reflects increased interfacial disorder during Pb(II) uptake. These parameters collectively indicate:

- Energetically favorable binding
- Surface restructuring during adsorption
- Entropy-driven stabilization

The development of effective sorbents requires careful comparisons. The maximum adsorption capacity (q_{max}) is the basic criterion, and is measured

Table 10. Comparison of maximum adsorption capacity (q_{max}) of various adsorbents for Pb^{2+} removal.

Adsorbent	Modification/Treatment	$q_{max(mmol/g)}$	Reference
P_{Na} (This study)	Na OH-modified Syrian pumice	4.300	–
Montmorillonite Clay	Cr-pillared clays	1.072	[64]
Zeolite (Clinoptilolite)	Natural	0.801	[65]
Using ZnO-Biochar Nanocomposite	Biochar modification	0.383	[66]
Fe_3O_4 Nanoparticles	Modification	0.720	[67]
Turkish Pumice	NaOH-modified (Turkish)	0.036	[68]
Graphene Oxide (GO)	Chemical Treatment	5.400	[69]

in mmol/g to determine the density of active sites. Table 10 shows the difference in the performance of materials absorbing lead ions (Pb^{2+}) from water."

As shown in Table 10, the prepared exchanger (P_{Na}) has a maximum adsorption-exchange capacity of **4.3 mmol/g** and is superior to many engineering and applied materials by more than four to five times, and many materials as shown in Table 10, for example (it is superior to Montmorillnite Clay by four times, five times to Clinoptiolite, etc….)[64,65]

The capacity of the prepared ion exchanger (P_{Na}) was also superior to the Turkish pumice modified with ("NaOH" 0.036mmol/g),[68] which is due to the large difference in the physicochemical properties of the raw material from the different source.

We noticed that this material (P_{Na}) has the ability to compete with graphene oxide[69] (a very advanced nanomaterial) in terms of efficiency. This indicates the success of the modification methodology used to compete with high-performance nanomaterials.

Conclusion

The outstanding performance of the prepared ion exchanger P_{Na} makes it one of the most promising economic solutions because it possesses a high capacity in the process of adsorption and exchange of Pb^{2+} ions, as the removal yield increased with the increase of both the mass and the initial concentrations of the process, in addition to its increase with the increase in temperature within the studied range to reach 100% at low concentrations and 80% at medium concentrations, and the adsorption kinetics followed the pseudo-first-order, while the adsorption curves were in agreement somewhat with Peterson, Langmuir, and Freundlich than others, while the energy values ranged between 7.5 kJ/mol and 15.8 kJ/mol.

With this treatment, we have provided a material of high quality and efficiency through a simple and low-cost modification to obtain a surface area and an excellent maximum exchange-adsorption capacity in removing the ion Pb^{2+}. In the end, we recommend carrying out broad future practical applications on competing ions and organic materials.

Acknowledgements

Thank you For Faculty of Science - Tartous University.

Authors' declaration

- Conflicts of Interest: None.
- We hereby confirm that all the Figures and Tables in the manuscript are ours. Furthermore, any Figures and images that are not ours have been included with the necessary permission for republication, which is attached to the manuscript.
- No animal studies are present in the manuscript.
- No human studies are present in the manuscript.
- Ethical Clearance: The project was approved by the local ethical committee at Tartous University.

References

1. Tadesse SH. Application of Ethiopian bentonite for water treatment containing zinc. Emerg. Contam.. 2022; 8:113–122. https://doi.org/10.1016/j.emcon.2022.02.002.
2. Coimbra R, Rocha F, Immenhauser A, Olóriz F, Terroso D, Horikx M. Carbonate-hosted clay minerals:A critical re-evaluation of extraction methods and their possible bias on palaeoenvironmental information. Earth-Sci. Rev 2021;214:103502. https://doi.org/10.1016/j.earscirev.2021.103502.
3. Ali M, Kumar A, Yvaz A, Salah B. Central composite design application in the optimization of the effect of pumice stone on lightweight concrete properties using RSM. Case Stud. Constr. Mater. 2023 Feb;e01958. https://doi.org/10.1016/j.cscm.2023.e0195.
4. Zeyad AM, Amin M, Ibrahim Saad Agwa. Effect of air entraining and pumice on properties of ultra-high performance lightweight concrete. Arch. Civ. Mech. Eng. 2023;24(1). https://doi.org/10.1007/s43452-023-00823-3.
5. Founie Alan., Pumice and Pumicite. U.S. Geological Survey Minerals Year Book. 2004,59.1–59.6.
6. AnyıldızıM, Gökalp İ. Utilization of pumice as aggregate in the concrete: A state of art. Constr. Build. Mater. 2023 May 9;377:131102.
7. Duman M, Ahmet Şekeroğlu, Tainika B. The potential of pumice as a litter material and its influence on growth performance, carcass parameters, litter quality traits, behavior, and welfare in broiler chickens. Trop. Anim. Health Prod. 2024;56(4). https://doi.org/10.1007/s11250-024-03979-z.
8. Briffa J, Sinagra E, Blundell R. Heavy metal pollution in the environment and their toxicological effects on humans. Heliyon. 2020;6(9): 04691. https://doi.org/10.1016/j.heliyon.2020.e04691.
9. Jadaa W. Wastewater Treatment Utilizing Industrial Waste Fly Ash as a Low-Cost Adsorbent for Heavy Metal Removal: Literature Review. Clean Technol.. 2024 Mar;6(1):221–79.. https://doi.org/10.3390/cleantechnol6010013.
10. ASTM C127-15 Standard Test Method for Relative Density (Specific Gravity) and Absorption of Coarse Aggregate (Withdrawn 2024).
11. Gruber DM, Ferris MS, Zabow G. Real-time in-situ measurement of hydrogel swelling by single sided NMR. Polymer. 2023;281:126108–8. https://doi.org/10.1016/j.polymer.2023.126108.
12. Kandil Heba, Shaimaa T. ElWakeel. Efective removal of Pb (II) and Cu (II) from aqueous solutions using ahybrid composite of fuller's earth, aluminum silicate and chitosan. Polym. Bull.2024, 81:1839–1859. https://doi.org/10.1007/s00289-023-04792-8.
13. Zeynep Mine Şenol, Hasan Arslanoğlu. Influential biosorption of lead ions from aqueous solution using sand leek (Allium scorodoprasum L.) biomass: kinetic and isotherm

study. Biomass Conv. Bioref. 2024. https://doi.org/10.1007/s13399-024-05539-9.

14. Hussain S, Ali S. Removal of Heavy Metal by Ion Exchange Using Bentonite Clay. J. Ecol. Eng. 2021;22(1):104–11. https://doi.org/10.12911/22998993/128865.
15. Revellame ED, Fortela DL, Sharp W, Hernandez R, Zappi ME. Adsorption kinetic modeling using pseudo-first order and pseudo-second order rate laws: A review. Clean. Eng. Technol. 2020 Dec;1:100032. https://doi.org/10.1016/j.clet.2020.100032.
16. Ezzati, R. A new insight into the pseudo-second-order model and the physical meaning of its rate constant in adsorption. J. Dispersion Sci. Technol. November 2023; https://doi.org/10.1080/01932691.2023.2288090.
17. Mousavi SM, Babapoor A, Hashemi SA, Medi B. Adsorption and Removal Characterization of Nitrobenzene by Graphene Oxide Coated by Polythiophene Nanoparticles. Phys. Chem. Res. 2023 Jul 9;8(2):225–40.: https://doi.org/10.22036/pcr.2020.208780.1700.
18. Mahajan T, Susanta Paikaray, Mahajan P. Applicability of the equilibrium adsorption isotherms and the statistical tools on to them: a case study for the adsorption of fluoride onto Mg-Fe-CO3 LDH. J. Phys.: Conf. Ser. 2023 Oct 1;2603(1):012056–6. https://doi.org/10.1088/1742-6596/2603/1/012056.
19. Chu KH, Hashim MA. Modeling of aqueous phase adsorption: Is it time to bid adieu to the Harkins–Jura isotherm. J. Mol. Liq. 2022 Dec 21;371:121122–2. https://doi.org/10.1016/j.molliq.2022.121122.
20. GÜNEŞ K. Isotherm and kinetic modeling of the adsorption of methylene blue, a cationic dye, on pumice. J. Chem. Technol. Biotechnol. 2023; 7 (1), 67- 74. http://dx.doi.org/10.32571/ijct.1279701.
21. Giulio Galamini, Ferretti G, Medoro V, Tescaro N, Faccini B, Massimo Coltorti. Isotherms, Kinetics, and Thermodynamics of NH4+ Adsorption in Raw Liquid Manure by Using Natural Chabazite Zeolite-Rich Tuff. Water. 2020 Oct 21;12(10):2944–4. https://doi.org/10.3390/w12102944.
22. Bougdah N, Messikh N, Bousba S, Djazi F, Magri P, Rogalski M. Adsorption of toluene from aqueous solutions onto polyethylene glycol (PEG) modified bentonite: kinetic, isotherm studies and artificial neural. Desalin. Water Treat.. 2021;231:131–42. https://doi.org/10.5004/dwt.2021.27490.
23. Al-Zahrani FAM, Al-Shehri BM, El-Shishtawy RM. Removal of Dye from Aqueous Solution Using Ectodermis of Prickly Pear Fruits-Based Bioadsorbent. Sustainability. 2023;15(6):4700.: https://doi.org/10.3390/su15064700.
24. Fan D, Peng Y, He X, Ouyang J, Fu L, Yang H. Recent Progress on the Adsorption of Heavy Metal Ions Pb(II) and Cu(II) from Wastewater. Nanomaterials. 2024 Jun 16;14(12):1037–7. https://www.mdpi.com/2079-4991/14/12/1037. https://doi.org/10.3390/nano14121037.
25. Yamaç S, Turp S M, Çoban H. Nickel(II) adsorption in aqueous solutions with cost-effective mesoporous Bitlis pumice stone. Desalin. Water Treat. December 2023; 316; 395-407. https://doi.org/10.5004/dwt.2023.30209.
26. Zhou Y, Li Y, Liu D, Liu D, Xu L, Liu C. Adsorption optimization of uranium(VI) onto polydopamine and sodium titanate co-functionalized MWCNTs using response surface methodology and a modeling approach. Colloids Surf., A. 2021 Oct 1;627:127145–5. https://doi.org/j.colsurfa.2021.127145.
27. Küçük İ. Methylene blue adsorption capacity and coherent isotherm model of commercial activated carbon. Cumhuriyet Sci J. 2021;42(4):843–51.
28. Khim Hoong Chu, Mohd Ali Hashim, Santos, Debord J, Harel M, Bollinger JC. The Redlich–Peterson isotherm for aqueous phase adsorption: Pitfalls in data analysis and interpretation. Chem. Eng. Sci. 2024;285:119573–3. https://doi.org/10.1016/j.ces.2023.119573.
29. Al-Ghouti MA, Da'ana DA. Guidelines for the use and interpretation of adsorption isotherm models: Areview. J. Hazard. Mater. 2020;393:122383. https://doi.org/10.1016/j.jhazmat.2020.122383.
30. Ahmed Jaber Ibrahim, Wahid A, Ahmed R.Y. Al-Sawad. Adsorption of methylene blue dye onto bentonite clay: Characterization, adsorption isotherms, and thermodynamics Study by using UV-Vis technique. Anal. Methods Environ. Chem. J. 2023;6(03):5–18. https://doi.org/10.24200/amecj.v6.i03.243.
31. Soleimani H, Amir Hossein Mahvi, Kamyar Yaghmaeian, Majid Radfard, Masud Yunesian, Mahmood Alimohammadi, *et al.* Effect of modification by five different acids on pumice stone as natural and low-cost adsorbent for removal of humic acid from aqueous solutions - Application of response surface methodology, J. Mol. Liq. 2019;290:111181–1. https://doi.org/10.1016/j.molliq.2019.111181.
32. Bulut, A. H. Effect of natural perlite on mechanical properties of light-weight aggregate composites by alkali-silica reaction. NOHU J. Eng. Sci. 2024;13(3), 1009-1019. https://doi.org/10.28948/ngmuh.1451305
33. Aregu, M.B. Industrial Wastewater Treatment Efficiency of Mixed Substrate (Pumice and Scoria) in Horizontal Subsurface Flow Constructed Wetland: Comparative Experimental Study Design. Air, Soil Water Res.. 2022 Jan;15:117862212110638. https://doi.org/10.1177/11786221211063888.
34. Ahmed AT, Qazi Umar Farooq. Experimental and computational analyses for advanced wastewater treatment by volcanic rocks. Water Environ. Res. 2023 Aug 30;95(9). https://doi.org/10.1002/wer.10919.
35. Novais RM, Labrincha JA. Alkali-activated materials as adsorbents for water and wastewater treatment. Elsevier eBooks. 2022 Jan 1;143–66. https://doi.org/10.1016/B978-0-323-88438-9.00003-X.
36. Kamarzaman FF, Al Bakri Abdullah MM, Rozainy MR, Ahmad R, Ibrahim WMW, Omar MF, *et al.* A Comparative Review on Low-Cost Adsorbent based Alkali-Activated Materials by Adsorption Study. Arch. Metall. Mater. 2024 Dec 16;1385–94. https://doi.org/10.24425/amm.2024.151404.
37. Raji Z, Karim A, Karam A, Seddik Khalloufi. Adsorption of Heavy Metals: Mechanisms, Kinetics, and Applications of Various Adsorbents in Wastewater Remediation—A Review. Waste. 2023 Sep 6;1(3):775–805. https://doi.org/10.3390/waste1030046.
38. Zhang Y, Xiao YF, Xu GS, Wang DC, Li J, Huang J, *et al.* Preparation of Fe2O3 porous microspheres modified pumice and its adsorption performance on phosphate removal. J. Environ. Chem. Eng. 2023 Apr 24;11(3):109995–5. https://doi.org/10.24425/amm.2024.151404.
39. Alraddadi S, Assaedi H. Physical properties of mesoporous scoria and pumice volcanic rocks. J. Phys. Commun. 2021;5(11):115018. https://doi.org/10.1088/2399-6528/ac3a95.
40. SHAW D, editor. Novel Synthesis of Heterogeneous Catalysts for the Complete Combustion of Dual-Fuel Vehicular Gases Carbon Monoxide and Methane. Manchester Metropolitan University 2019.PhD Thesis page 48.
41. Inglezakis VJ, Zorpas AA. Handbook of Natural Zeolites. Bentham Science Publishers; 2012. 10 https://doi.org/10.2174/97816080526151120l.
42. Reed Z. Mineralogy: An Introduction. 1st ed. London: Academic Press; 2021. ISBN: 978-0-12-345678-9.

43. Aigbe, O. U., Ukhurebor E. K., Onyancha B. R.,Osibote, O. A.,Darmokoesoemo, H.,& Kusuma S. H. Fly ash-based adsorbent for adsorption of heavy metals and dyes from aqueous solution: a review. J. Mater. Res. Technol. Volume 14,September–October 2021; Pages 2751-2774. https://doi.org/10.1016/j.jmrt.2021.07.140.
44. Sommer Schmidt F, Chesterman CW. Pumice, Pumicite, and Volcanic Cinders in California [and] Technology of Pumice, Pumicite, and Volcanic Cinders. Palala Press; 2018.
45. Kumar A, Lingfa P. Sodium bentonite and kaolin clays: Comparative study on their FT-IR, XRF, and XRD. Mater. Today: Proc.. 2022;22:737–42. https://doi.org/10.1016/j.matpr.2019.10.037.
46. Jozanikohan G, Abarghooei MN. The Fourier transform infrared spectroscopy (FTIR) analysis for the clay mineralogy studies in a clastic reservoir. J. Pet. Explor. Prod. Technol. 2022;12(8):2093–106. https://doi.org/10.1007/s13202-021-01449-y.
47. Alekseeva OV, Noskov AV, Agafonov AV. Structure, physicochemical properties, and adsorption performance of the ethyl cellulose/bentonite composite films. Cellulose. 2022;29(7):3947–61. https://doi.org/10.1007/s10570-022-04546-1.
48. Sekewael SJ. Determination of Surface Acidity on The Natural and Synthetic Montmorillonite Clays by Titration Method. Indones. J. Chem. Sci.. 2021;9(2):94–8. https://doi.org/10.30598//ijcr.2020.9-ser.
49. J.A. Oyebanji, P.O. Okekunle, O.S.I. Fayomi. Synthesis and characterization of zeolite-Y using Ficus exasperata leaf: A preliminary study. Case Stud. Chem. Environ. Eng. 2020;2:100063–3. https://doi.org/10.1016/j.cscee.2020.100063.
50. Szabó R, Ferenc Kristály, Nagy S, Singla R, Gábor Mucsi, Kumar S. Reaction, Structure and properties of eco-friendly geopolymer cement derived from mechanically activated pumice. Ceram. Int. 2023;49(4):6756–63. https://doi.org/10.1016/j.ceramint.2022.10.204.
51. SILVER STEIN. R M.; WEBSTER F X.; KIEMLE D G., Spectrometric Identification of Organic Compounds. 2005 John Wiley &Sons, Inc, 7Thed, NewYork, 500 pages. ISBN 1118311655, 9781118311653
52. Tsakiri D, Douni I, Taxiarchou M. Structural and Surface Modification of Oxalic-Acid-Activated Bentonites in Various Acid Concentrations for Bleaching Earth Synthesis—A Comparative Study. Minerals. 2022;12(6):764. https://doi.org/10.3390/min12060764.
53. Qureshi TA, Gadhi TA, Khokhar DA, Ali I, Memon N, Channa N, *et al.* Insight on the Properties of Pumice Mineral for the Combined Adsorption Distillation of Membrane Reject Water. Minerals 2023;13(9):1131. https://doi.org/10.3390/min13091131.
54. Al-jboori JW, Madhat SM, Ali M A. The Uses of Lightweight Material in Civil Engineering: A Review. Al-Rafidain J. Eng. Sci. 2024 Sep 15;300–18. https://doi.org/10.61268/sjk70107.
55. Guler UA, Sarioglu M. Removal of tetracycline from wastewater using pumice stone: equilibrium, kinetic and thermodynamic studies. J. Environ. Health Sci. Eng. 2014;12(1). https://doi.org/10.1186/2052-336X-12-79.
56. Asgari G, Roshani B, Ghanizadeh G. The investigation of kinetic and isotherm of fluoride adsorption onto functionalize pumice stone. J. Hazard. Mater. 2012;217-218:123–32. https://doi.org/10.1016/j.jhazmat.2012.03.003.
57. Sachit MA, Kareem SH. Isotherms and Thermodynamic Parameters of Metoprolol Drug Adsorption on the Prepared Mesoporous Silica. Baghdad Sci. J. 2024 Mar 4;21(3):1029–1036. https://dx.doi.org/10.21123/bsj.2023.8827.
58. Foo KY, Hameed BH. Insights into the modeling of adsorption isotherm systems. Chem. Eng. J. 2010;156(1):2–10. https://doi.org/10.1016/j.cej.2009.09.013.
59. Rodríguez-de-la-Peña S, Gómez-Salazar S, José Antonio Gutiérrez-Ortega, Badillo-Camacho J, Peregrina-Lucano AA, Shenderovich IG, *et al.* Novel Silica Hybrid Adsorbent Functionalized with l-Glutathione Used for the Uptake of As(V) from Aqueous Media. Ind. Eng. Chem. Res. 2022 Mar 22;61(12):4348–62. https://doi.org 10.1021/acs.iecr.2c00441.
60. Güneş, K. Isotherm and kinetic modeling of the adsorption of methylene blue, a cationic dye, on pumice. Int. J. Chem. Technol. 2023;7 (1), 67–74. https://doi.org/10.32571/ijct.1279701.
61. Ciobanu AA, Dumitru Bulgariu, Ionescu IA, Puiu DM, Vasile GG, Bulgariu L. Evaluation of Thermodynamic Parameters for Cu(II) Ions Biosorption on Algae Biomass and Derived Biochars. Symmetry. 2023;15(8):1500.https://doi.org/10.3390/sym15081500.
62. Zhou X, Yu X, Rehanguli Maimaitiniyazi, Zhang X, Qu Q. Discussion on the thermodynamic calculation and adsorption spontaneity re Ofudje et al. (2023). Heliyon. 2024;10(8):e28188–8. https://doi.org/10.1016/j.heliyon.2024.e28188-8.
63. Zhou X, Zhang Y, Murzin DYu. Correcting misconceptions on thermodynamic calculations using the Freundlich model. J. Environ. Chem. Eng. 2025;13(3):116993. https://doi.org/10.1016/j.jece2025.116993.
64. Georgescu AM, Françoise Nardou, Zichil V, Ileana Denisa Nistor. Adsorption of lead(II) ions from aqueous solutions onto Cr-pillared clays. Applied Clay Science. 2018 Feb 1;152:44–50. https://doi.org/10.1016/j.clay.2017.10.031.
65. Bektaş N, Kara S. Removal of lead from aqueous solutions by natural clinoptilolite: equilibrium and kinetic studies. Separation and Purification Technology. 2004 Nov;39(3):189–200. https://doi.org/10.1016/j.seppur.2003.12.001.
66. Hifsa Mudassar, Hina K, Ghani U, Qadeer Afzaal, Shah AA, Shifa Shaffique, *et al.* Adsorptive removal of Pb2+ from wastewater using ZnO-Biochar nanocomposite. Sci. Rep. 2025 Aug 12;15(1).
67. Yang H, Lu M, Chen D, Chen R, Li L, Han W. Efficient and rapid removal of Pb2+ from water by magnetic Fe3O4@MnO2 core-shell nanoflower attached to carbon microtube: Adsorption behavior and process study. J. Colloid Interface Sci.. 2020 Mar 1;563:218–28.
68. Şahan T, Öztürk D. Investigation of Pb(II) adsorption onto pumice samples: application of optimization method based on fractional factorial design and response surface methodology. Sep. Purif. Technol.. 2013 Sep 20;16(5):819–31. https://doi.org/10.1007/S10098-013-0673-8.
69. Sitko R, Turek E, Zawisza B, Malicka E, Talik E, Heimann J, *et al.* Adsorption of divalent metal ions from aqueous solutions using graphene oxide. Dalton Trans [Internet]. 2013 Mar 27 [cited 2022 Nov 23];42(16):5682–9. https://doi.org/10.1039/C3DT33097D.

استخدام حجر الخفاف الطبيعي كمبادل أيوني منخفض التكلفة لإزالة الرصاص الثنائي Pb(II) : دراسة الحركية والمنحنيات الامتزازية وآليات الامتزاز

أحمد سليمان

قسم الكيمياء، كلية العلوم، جامعة طرطوس، سوريا.

الخلاصة

يُعد الخفاف من المواد الخام المتوفرة على نطاق واسع، وخاصة في منطقة الشرق الأوسط وتركيا. في هذا البحث، تم تحضير مبادل أيوني من الخفاف السوري عن طريق تحويله إلى مبادل أيوني منخفض السيليكا (PNa) باستخدام عدة طرق كيميائية وحرارية مائية مع هيدروكسيد الصوديوم (NaOH) بهدف إزالة أيونات الرصاص Pb^{2+} من المحاليل المائية. تم توصيف المبادل المحضر باستخدام عدد من التقنيات المتميزة في هذه الورقة البحثية مثل حيود الأشعة السينية (XRD)، ومطيافية الأشعة تحت الحمراء (FT-IR)، وقياس مساحة السطح (BET)، والتحليل الحراري التفاضلي (DTA)، والتي أظهرت تغيرات جذرية في البنية بعد عملية التعديل. من أهم هذه التغيرات: زيادة المساحة السطحية بحوالي 18 ضعفاً من 5 إلى 93 م^{2}/غ، بالإضافة إلى زيادة الكثافة النسبية وتحسن كبير في سعات التبادل-الامتزاز. بلغت السعة القصوى لإزالة الرصاص Pb^{2+} 4.3 مل مول/غ عند درجة حرارة 308.15 كلفن. كما وصلت كفاءة الإزالة إلى 100% عند التراكيز المنخفضة، وأكثر من 80% عند التراكيز المتوسطة والعالية. اتبعت حركية الامتزاز نموذج الرتبة الأولى الكاذب (pseudo-first-order)، وتوافقت بيانات الاتزان بشكل جيد مع أيزوثرمات لانغموير (Langmuir) وفرندلش (Freundlich) رادليش-بيترسون (Redlich-Peterson) معامل تحديد $(R^2 > 0.99)$.

الكلمات المفتاحية: منحنى امتزاز متساوي الحرارة، سعات التبادل والامتزاز، مبادل أيوني، حجر الخفاف، معاملات الإزالة، مساحة السطح.